LED based solar simulator to study photochemistry over a wide temperature range in the large simulation chamber AIDA

Magdalena Vallon, Linyu Gao, Feng Jiang, Bianca Krumm, Jens Nadolny, Junwei Song, Thomas Leisner and Harald Saathoff

5   Institute of Meteorology and Climate Research, Karlsruhe Institute of Technology, 76344 Eggenstein-Leopoldshafen, Germany

Correspondence to: Harald Saathoff (Harald.Saathoff@kit.edu)

Abstract.

A light source has been built at the simulation chamber AIDA (Aerosol Interactions and Dynamics in the Atmosphere) at the

10   Karlsruhe Institute of Technology, simulating solar radiation at ground level. Instead of full spectra light sources, it uses a combination of LEDs with a narrow emission spectrum, resulting in a combined spectrum similar to the solar spectrum between 300 and 530 nm. The use of LEDs leads to an energy-efficient, robust and versatile illumination concept. The light source can be used over a wide temperature range down to -90°C, is adjustable in intensity and spectral width as well as easily adjustable to new technological developments or scientific needs. Characterization of the illumination conditions shows a vertical

15   intensity gradient in the chamber. The integral intensity corresponds to a NO_2 photolysis frequency $j(NO_2)$ of $(1.58 \pm 0.21$ $(1\sigma)) \times 10^{-3}$ s^{-1} for temperatures between 213 and 295 K. At constant temperature, the light intensity is stable within $\pm 1\%$. While the emissions of the different LEDs change with temperature, they can be adjusted, thus it is possible to adapt the spectrum for different temperatures. Although, the illumination of the simulation chamber leads to an increase of 0.7 K h^{-1} of the mean gas temperature, it is possible to perform experiments with aqueous droplets at relative humidities up to ≤95% and

20   also above water or ice saturation with corresponding clouds. Additionally, temperature and wavelength dependent photolysis experiments with 2,3-pentanedione have been conducted. The photolysis of 2,3-pentanedione occurs mainly between 400 and 460 nm resulting in a mean photolysis frequency of $(1.03 \pm 0.15) \times 10^{-4}$ s^{-1} independent of temperature in the range 213-298 K with a quantum yield of 0.36 ± 0.04. In contrast the yield of the two main photolysis products, acetaldehyde and formaldehyde, decreases with temperature. Furthermore, the light source was applied to study the photochemistry of aerosol

25   particles. For the atmospheric brown carbon proxy compound 3,5-diacetyl-2,4,6-trimethyl-1,4-dihydropyridine photochemical reaction products were identified. In aerosol particles containing iron oxalate as photosensitizer the photosensitized degradation of organic acids (pinic and pinonic acid) was studied. Although, the light source only generates about 1/3 of the maximum solar irradiation at ground level with a substantial intensity gradient throughout the simulation chamber it could be shown that this type of light source allows reproducible experiments over a wide range of simulated atmospheric conditions

30   and with a large flexibility and control of the irradiation spectrum.

1 Introduction

The interaction of light with the atmosphere is an important factor in understanding the physical and chemical processes influencing air quality and our climate. Alongside direct radiative effects, the interaction with clouds and aerosols, a mixture

35 of either solid or liquid particles with gas, are significant. From a chemical viewpoint, light enables, besides the thermodynamic the photochemical pathway by lifting electrons in a higher energy level, thereby exiting the molecules. This leads to a multitude of reaction pathways which, without light would not be possible. Typical photochemical reactions like the formation of ozone and OH-radicals or the fragmentation of halocarbon compounds have been studied widely in the last few decades, now offering a good understanding for the big picture. For the at least 10^4-10^5 different organic compounds in the atmosphere the picture

40 looks different and additional research is much-needed (Goldstein, 2007). The lack of a proper understanding of the influence of such compounds can also be seen in the high uncertainty of interaction of aerosols with light in the ICCP report (Stocker, 2013).

In principal photochemical reactions in the atmosphere can not only be categorized in inorganic and organic processes but also if they take place in gas or particle phase. Some substances are even only able to absorb in the ultraviolet to visible (UV-Vis)

45 or enlarge their absorption cross section considerably by adsorbing at particles, thus breaking the symmetry of their molecule orbitals (Navea, 2017). A well-studied example is the chemisorption of NO_3^- to Al_2O_3 surfaces and subsequent photolytic reaction to NO_2 (Baltrusaitis, 2007; Rubasinghege, 2009). But molecules do not have to fragment directly, especially more complex organic molecules can absorb the photon and transfer the excess energy to surrounding molecules leading to an enhanced fragmentation of substances which cannot absorb photons in the respective wavelength range themselves. Such

50 molecules are called photosensitizers (Herrmann, 2015; George, 2015). In seawater, chlorophyll and humic acids take on this role. At the sea surface chlorophyll absorbs photons and reduces Cl^- to the reactive Cl atoms (Reeser, 2009) and isoprene is being produced from nonanoic acids under the influence of humic acids (Ciuraru, 2015). Also aldehydes, acids (Rossignol, 2014; Monge, 2012; Aregahegn, 2013; Fu, 2015), metals and metal oxides have shown to act as photosensitizers in atmospherically relevant processes (overviews regarding the latter two can be found in Herrmann, 2015 and George, 2015).

55 By an increase of oxidation through solar irradiation more compounds with a low vapour pressure are likely to be formed also in the gas phase, thus forming new particles or condensing on existing particles. Consequently, light is not only contributing to the aging but also to the formation of new particles, increasing particle phase and consequently reactions which are only possible in liquid or solid phases (Navea, 2017). A lack of proper research methods to simulate atmospheric photochemistry therefore underestimates the formation of various, possibly harmful, components.

60 Apart from field measurements, controlled experiments in cloud simulation chambers offer the possibility to understand the atmospheric processes. One of these simulations chambers is the AIDA-chamber (Aerosol Interactions and Dynamics in the Atmosphere) at the Institute of Meteorology and Climate Research at the Karlsruhe Institute of Technology (KIT). It is one of the largest atmospheric simulation chamber which has a solid chamber wall, allowing temperatures down to -90°C, as well as cloud formation by adiabatic expansion (Möhler, 2003; Saathoff. 2003). The volume and temperature stability offers the

65   possibility for long-term experiments with aerosols. Until now it didn't have the possibility to simulate solar irradiation, however, and as it has a solid aluminium casing it cannot use the natural sunlight like the Teflon chambers SAPHIR in Jülich (Bohn and Zilken, 2005; Rohrer et al., 2005), EUPHORE in Valencia (Wiesen, 2001; Zádor et al. 2006) or HELIOS in Orléans (Ren et al., 2017). To simulate some aspects of the atmospheric chemistry processes it is possible to generate ozone or OH radicals without a light source. But this only allows to simulate a limited part of atmospheric photochemistry. Other similar

70   chambers have solved this issue by using either xenon arc lamps (CESAM chamber; Wang et al., 2011) fluorescent tubes or black light (PACS-C3: Platt et al., 2013; Fankhauser et al., 2020) or single wavelength LEDs (CLOUD-chamber: Lehtipalo et al., 2018). LEDs and fluorescent tubes have the advantages that they are easy to use, emit less heat and are relatively cost-efficient. Nevertheless, they are not emitting in the full spectral range of the photochemical relevant spectrum, which should start at around 300 nm depending on the atmospheric height (solar spectrum see supplementary information) and reach at least

75   until 500 nm to include photochemical reactions of chromophores found in organic matter (Sharpless, 2014). High-pressure xenon arc lamps on the other hand are emitting a spectrum similar to the solar spectrum with high intensities. However, they are difficult to handle due to their size and the risk of imploding light bulbs. Additionally the spectrum is often too broad making it necessary to apply filters, blocking part of the UV and the infrared radiation (Wang, 2011). So none of these solutions were favourable for the illumination of the AIDA chamber.

80   In the following we will describe the implementation of a newly designed light source for the AIDA chamber as well as the spectral characterization and photochemical characterization by the photolysis of NO_2. Additionally, the results of temperature and wavelength dependent photolysis experiments of 2,3-pentanedione, will be presented and a first insight will be given into the photochemical aging of a brown carbon proxy and photosensitized decomposition of atmospherically relevant organic acids.

85   **2 Experimental overview**

2.1 AIDA aerosol and cloud simulation chamber

The AIDA simulation chamber at KIT is designed to simulate atmospheric conditions in the temperature range of -90 °C to + 60 °C. It is comprised of an aluminium cylinder with a 4m inner diameter and a torispherical head and bottom, resulting in a 7.5 m high chamber with a volume of 84.5 m³ and an inner surface area of 103 m² (Saathoff, 2009). To recreate different

90   atmospheric pressures and to facilitate the cleaning of the chamber, the pressure inside the vessel can be adjusted between 0.01 hPa and 1500 hPa. Various flanges and lances are implemented and allow the addition of synthetic air, chemicals or aerosols as well as the mounting of different measurement instruments. By rotating with 400 revolutions per minute, a fan inside the chamber enables homogeneous dispersion of all components in less than 2 minutes. A more detailed description of the chamber can be found in Wagner et al., 2006, Saathoff et al., 2003 and Müller at al., 2012.

2.2 Instrumentation

For the spectral measurements three different UV-Vis-Spectrometer were used. For continuous monitoring during the experiments a UV-Vis Spectrometer (CCS200-Thorlabs) is connected via an optical fibre to the AIDA bottom looking inside the chamber via an off-axis parabolic mirror and through a quartz window. For the spatially resolved measurements inside the chamber two calibrated UV-Vis spectrometer with diffusor heads were used (SR900HS, Opsytec; LI-1800 LICOR). Please note, that the spectra measured with the fibre coupled spectrometer show a bias compared to the calibrated ones essentially significantly underestimating the UV wavelengths.

The concentrations of the trace gases were measured with different gas sensors. For nitrogen dioxide the cavity phase shift NO_2 Analyzer (AS32M Environment S. A.), for nitrogen oxide the chemiluminescence NO analyser (CLD 77AM Eco Physics) and for ozone the UV photometric ozone monitor (O3 41M Environment S. A.) were used. All of these gas sensors are connected to the chamber through FEP-tubes.

For the concentration measurements of 2,3-pentanedione and its reaction products, a proton transfer mass spectrometer (PTR-TOF-MS 4000, Ionicon, hereafter PTR-MS) was connected via SilcoNert coated stainless tubes to the AIDA chamber, measuring the gas phase continuously. The PTR-MS is a time-of-flight mass spectrometer, ionizing organic components by transferring a proton from H_3O^+ to the analyte (Romano et al., 2015; Yuan et al. 2017). Furthermore, the PTR-MS coupled with the particle inlet of CHARON (Chemical Analysis of Aerosol Online) can be alternatively switched between particle and gas phase for the particle phase measurement of semi-volatile compounds. In addition, a chemical ionization mass spectrometer (HR-ToF-CIMS, Aerodyne Inc., hereafter CIMS) ionizing with iodide (I^-) with high sensitivity for highly oxidized organic molecules. Its FIGAERO attachment (Filter Inlet for Gases and AEROsols) allows the sampling of aerosol particles on Teflon filters, the subsequent heating of the filters to 200°C to evaporate the particle phase components into the gas phase, and detection by the CIMS (Lopez-Hilfiker, 2014). To ensure gas phase analysis at the chamber throughout the experiments, aerosol filters were taken separately, stored at -20°C in individual containers and analysed as soon as the experiments were completed.

2.3 Experimental procedures

For all photochemical experiments the chamber was cleaned by evacuating and flushing repeatedly with synthetic air and ozone. Afterwards it was filled with a defined amount of water vapour and synthetic air (21 % O_2, 79 % N_2) generated by evaporating liquid nitrogen (class 2.2 (C/E), AirProducts) and liquid oxygen (4.8 – 99.998 Vol%, Basi).

For the NO_2-photolysis experiments, 40-70 ppb of NO_2 (1000.3 ppm NO_2 2.5 in N_2 5.0, Basi) were added to the chamber and illuminated for 40 min. The light source was operated at the highest intensity possible for every temperature.

For the photolysis of 2,3-pentanedione, 66-71 ppb and in one case 20 ppb of 2,3-pentanedione were added to the chamber either to the pure synthetic air or after a photochemical experiment with NO_2. For the temperature dependent photolysis experiments the light source was used in the same intensity for each temperature as for the corresponding temperature in the

photolysis of NO_2, illuminating for 60-65 min. Additionally 2,3-pentanedione was irradiated for intervals of 15 min using a different range of wavelengths for every interval.

For the photolysis of the brown carbon proxy two solutions were prepared each containing NH_4NO_3, $(NH_4)_2SO_4$ and 3,5-
130 diacetyl-2,4,6-trimethyl-1,4-dihydropyridine (hereafter DTDP). One solution contained a commercial DTDP (Sigma-Aldrich, 97%) (2.00 g/l NH_4NO_3, 1.221 g/l $(NH_4)_2SO_4$, 1.11 g/l DTDP) for the second solution the DTDP was prepared in the laboratory by using acetaldehyde (44.34 g/l, Acros Organics 99,5%), 2,4-pentanedione (100.22 g/l, Alfa Aesar 99%) and $(NH_4)_2SO_4$ (132.16 g/l) according to Kampf et al., 2016. In this way the atmospheric processes leading to the formation of the brown carbon proxy were imitated and potential by-products would also appear in the solution. The solutions were nebulized
135 into the chamber using an ultrasonic nebulizer (Synaptec) and illuminated for 120 min.

To mimic photosensitized decomposition of organic acids, a solution of NH_4NO_3, iron oxalate ($C_6Fe_2O_{12}$, Sigma-Aldrich) as the photosensitizer and pinonic (Acros Organics 98%) and pinic acid (~95% synthesized by University of Frankfurt) as atmospherically relevant organic acids, was nebulized in the chamber and illuminated twice, each time for one hour. As a reference the experiment was repeated with a solution of oxalic acid, pinonic acid and NH_4NO_3. A detailed overview of the
140 concentrations and experimental characteristics can be found in the supplementary information (Table S1).

3 Construction of the light source

The design criteria for the light source for the AIDA chamber were: (1) The spectrum of the light source should allow to mimic the solar spectrum in the troposphere, but should be variable in intensity and wavelength range, to allow simulation of different atmospheric heights as well as wavelength specific photolysis experiments. (2) The light source should affect the temperature
145 homogeneity and the leak tightness of the chamber as little as possible. It should work in the temperature range from 303 K to 183 K, be energy efficient, easy to handle, maintain and improve or adapt to new technical developments. With these, classical solutions like arc lamps or fluorescent tubes were ruled out. Instead, a light source was designed by using a combination of LEDs with a small full width at half maximum (FWHM) (~10-15 nm) and peak wavelengths from 305 nm to 528 nm. In total 3000 LEDs covering 11 different wavelengths were used, leaving out the longer wavelengths above 530 nm. All the LEDs
150 were tested beforehand to ensure their functionality at temperatures down to 183 K and their emission spectrum regarding changes with temperature and operating with different electric current was characterized. For the most part, spectral changes regarding the electrical current were minor and can be neglected. On the other hand, temperature changes are influencing the emission spectrum substantially. In general, a shift in the peak wavelengths of up to 5 nm could be observed while changing the ambient temperature from 298 K to 183 K. The intensity increased or decreased depending on the manufacturer and LED-
155 type by up to + 60% or – 50% (examples for LEDs with a wavelength of 340 nm and 365 nm are available in the supplement). For every LED-type which underwent a decrease in intensity, the reduction could be counteracted by increasing the electric current at the respective temperature. To prevent degradation of the LED-lenses due to aggressive chemicals, the light source was not installed inside the chamber but on top of the chamber on three aluminium heat sinks mounted above flanges with a

diameter of 500 mm (fig.1b-d). Each flange lid contains three CF flanges (VPCF200UVQ-L, VACOM) with quartz windows (Fused Silica, Corning HPFS 7980) with a thickness of 9 mm and a diameter of 200 mm each. Resulting in a total of 9 windows for the light to pass through into the chamber (see Fig.1a and c). The flanges are mounted at an angle of 14° on top of the chamber, so that the incoming light forms three conical radiation paths overlapping in the middle of the chamber. The different LED types were distributed as homogeneously as possible over the three flanges. The volume between the LEDs and the quartz windows is constantly flushed with dry nitrogen (20 l min^{-1}) during operation to avoid condensation of water and build-up of ozone, helping also with reducing the heat. To avoid unnecessary irradiation losses, stripes of eloxated aluminium mirrors (MIRO 4300UP, alanod) were installed between the windows and the LEDs and at the inner part of the 500 mm-flanges (see fig. 1b). The cooling rate of the heat sinks ((60 x 60) cm², JK 2907, Junior Kühlkörper GmbH) is enforced by 5 fans (8218 JH4, Ebmpapst) per heat sink, forcing the air through the gills of the heat sinks. To monitor the temperature of the LED boards, 28 temperature sensors (Pt1000) are placed on top of different boards. During operation the LED boards heat up to a maximum of 344 K at room temperature. All the electronical parts are connected to two 19" racks outside of the chamber isolation, containing all the necessary power supplies for the LEDs , the components to control the power supplies (cRio-9066, National Instruments), as well as the modules to process the temperature signals (NI-9226, NI-9264, NI-9476, NI-9209, NI-9221, National Instruments). A general connection scheme can be found in the supplementary information. The whole setup is controlled by a specifically written software (LabVIEW, National Instruments). It allows to control the LEDs intensity for every wavelength, reads the actually flowing electric current as well as the temperatures. Maximum values for the electric current and the temperatures can be set by the user, leading to an automatic shutdown of the light source if one of these values is exceeded. The UV-Vis spectrometer (CCS200, Thorlabs) installed at the bottom of the chamber, measuring constantly the light spectrum inside the chamber, serves as an additional control mechanism to ensure constant irradiation is achieved during the experiments.
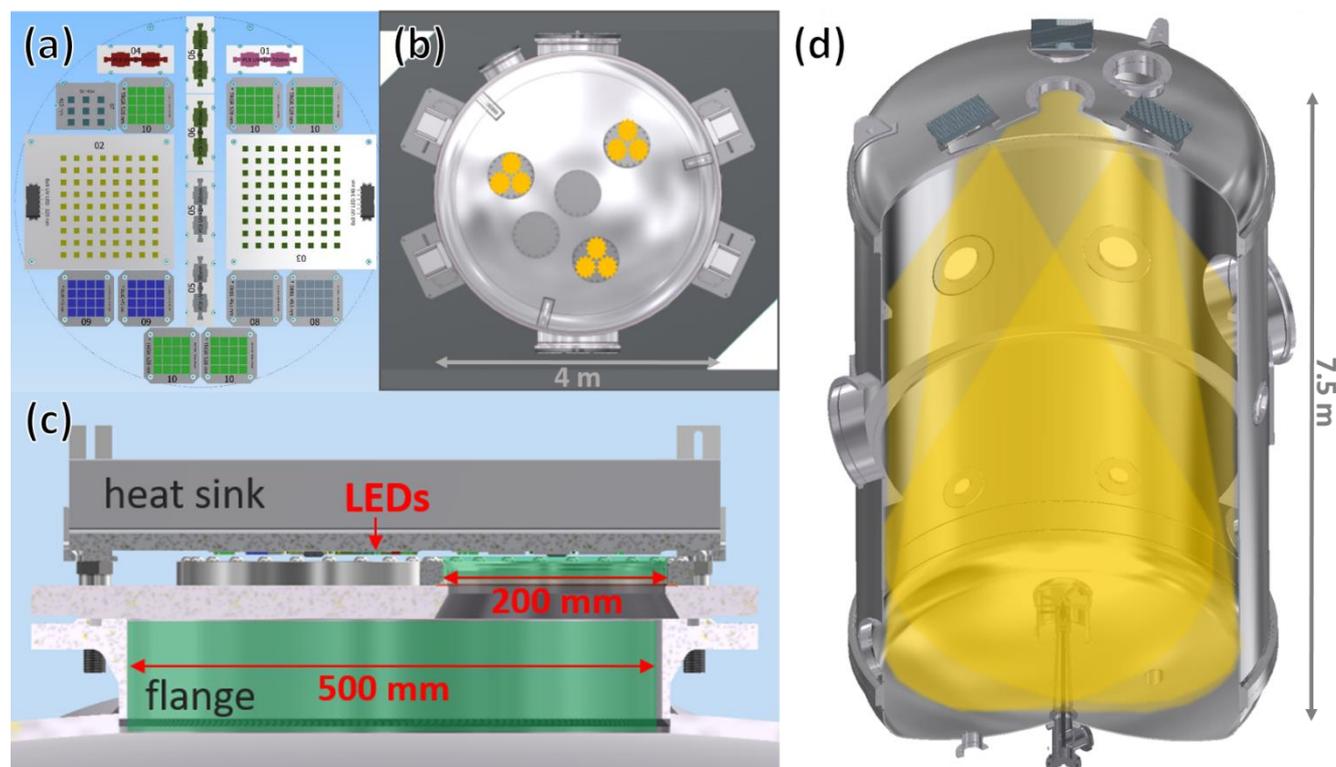
Figure 1: a) LED board placement matching one 200 mm window. b) Three of these patches are placed on one heat sink above the 500 mm flange with three 200 mm quartz windows. c) Placement of the flanges and the windows on top of AIDA. d) Placement of the light source in relation to the whole AIDA with corresponding light cones.

4 Characterisation of the light source

The total radiative output of all LEDs amounts to 1400 W, while the UV-LEDs have efficiencies of only ~2%, the LEDs with longer wavelengths reach efficiencies of 30 to 70%. The optical power is distributed over the different wavelengths and over the chamber cross-section. For a proper characterization of the illumination, spatially resolved spectral and integral actinometric measurements were performed.

4.1 Spectral and spacial characteristics

The combined emission of all the LEDs results in a spectrum, similar but not identical to the solar spectrum at ground level. Measurements in the centre of the chamber (see Fig. 2a) show that the spectral distribution matches the solar spectrum by overlapping of the single LED-spectra. Only at 357 nm and 440 nm are discrepancies due to the fact that LEDs with a peak wavelength in that region and high efficiency are, to our knowledge, not yet available. The intensity and to a lesser extent the spectral distribution is dependent on the position in the chamber. Due to the conical dispersion of the light the irradiated area increases quadratically and the intensity of the light reduces accordingly. This effect and the absorption of light on the walls

leads to strong vertical but smaller horizontal gradient in intensity. Measurements show that the light intensity in the centre of the chamber at about 1 m above ground level represents 45% of the intensity at a height of 4 m. This can be further divided into the different parts UV-B (280-315 nm), UV-A (315-400 nm) and visible light (400-620 nm). The absorption of light with shorter wavelengths by the chamber walls and flange collar, is stronger than for the light with longer wavelength, resulting in

200 a reduction of the UV-parts in comparison to the visible part. This is also in accordance with the reflectivity of non-oxidized aluminium which shows a maximum in reflectivity at around 400 nm (Bartl and Baranek, 2004) Comparing the values of the measurements at 1 m and 4 m the UV-B at 1 m represents 32 %, the UV-A represents 43% and the visible 47% of the values at 4 m. The absorption on the walls and the overlapping of the light cones in the middle of the chamber also lead to a slight radial intensity gradient (see Fig. 2b). At 1.20 m left and right to the chamber centre at 1 m height the light intensity is on

205 average 86% of the light intensity in the centre at the same height.
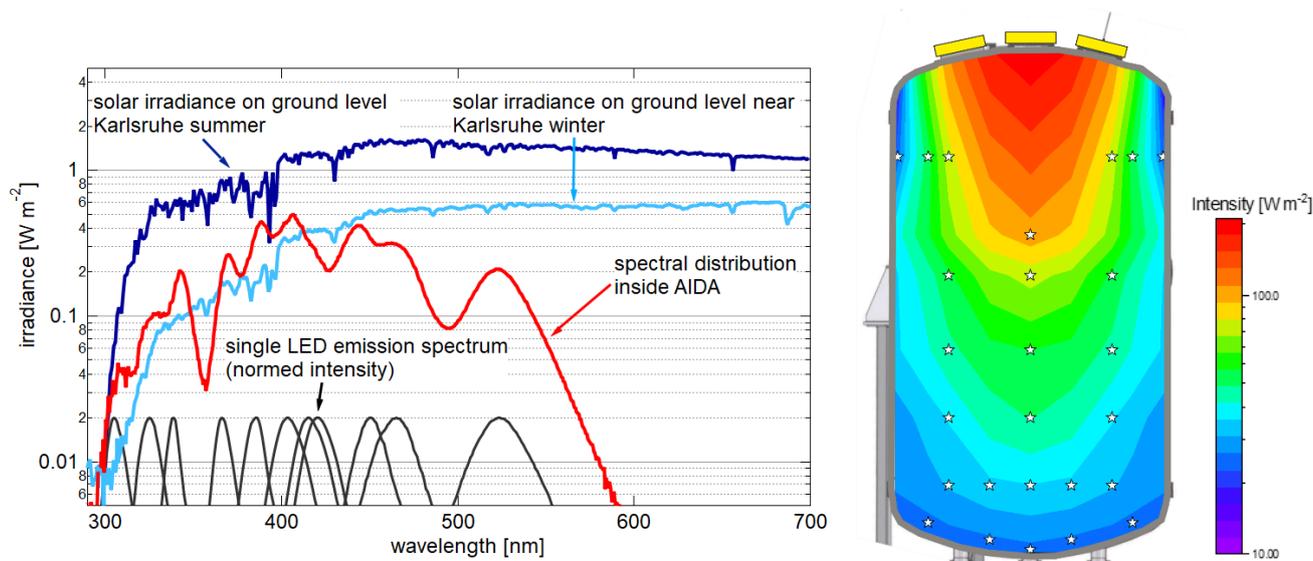
Figure 2: a) Light spectrum inside the AIDA chamber, measured at a central position at a height of 2.9 m above the chamber floor. Solar irradiance for winter was measured with a calibrated spectrometer at KIT. The solar irradiance for summer is calculated with the NCAR UCAR Quick TUV model (further information in the supplement). b) Light intensity distribution interpolated based on
210 **measurements at 26 different positions (white stars) inside the AIDA chamber.**

4.2 Stability of the light source

At a constant temperature, the emission of the light is also constant in intensity, thus offering reproducible illumination conditions. As the emission of the LEDs themselves is temperature dependant, the resulting spectra in the chamber change

215 slightly with temperature. This also leads to the effect that after switching on the LEDs it takes less than 3 min until the LEDs have reached a constant operating temperature. After this initial period the light emission remains constant within ± 0.02% (see Fig. 3b). This effect is less pronounced at warmer temperatures. The overall variability is less than 1% at constant temperature. Additionally the LEDs can be operated at higher electrical currents at lower temperatures, changing the emitted

spectrum further with typically higher emissions for lower wavelengths (cf. Fig. 3a). Alternatively, it would be possible to
220   apply lower currents at lower temperatures to keep the emission spectrum nearly constant compared to warmer conditions.
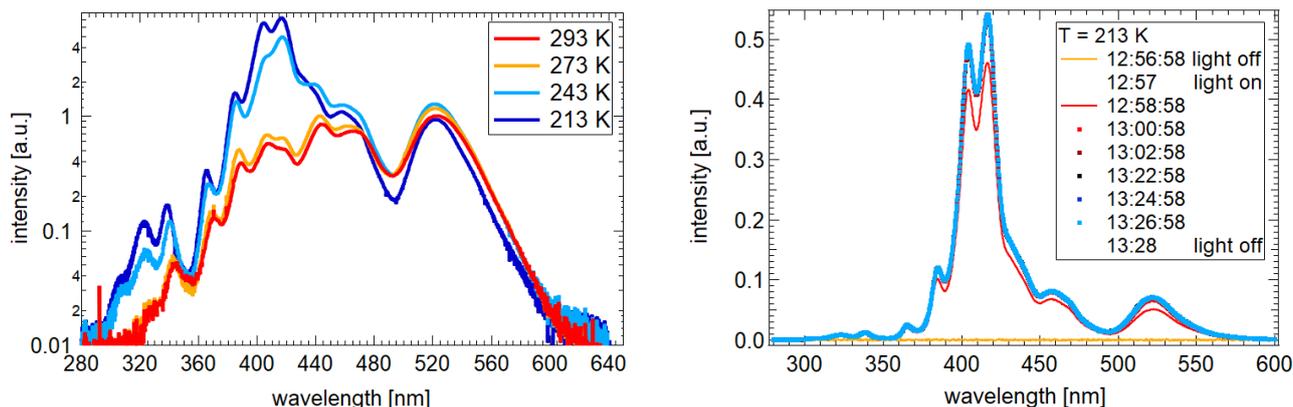
Figure 3: a) Spectra taken with the UV-Vis spectrometer at the bottom of the chamber at 4 different temperatures. The electrical settings for the LEDs for each temperature are different. In addition to the emission changes of the LEDs due to the temperature variation, this leads to different spectral distributions for each temperature. b) Spectra taken with the UV-Vis spectrometer at the
225   **bottom of the chamber over a time period of 30 min.**

4.3 Integral light intensity

The actinometric experiments, by using the photolysis of NO_2 inside the chamber, provide photolysis frequencies for every measured temperature and light setting. Thus offering reference values of the light intensity for comparison with other
230   simulation chambers or with solar irradiation. The photolysis of NO_2 can be described with the following three equations, neglecting further side reactions (Harvey et al., 1977; Holmes et al., 1973).

$$NO_2 + h\nu \overset{k_1}{\rightarrow} NO + O \qquad (R1)$$

$$O + O_2 + M \overset{k_2}{\rightarrow} O_3 + M \qquad (R2)$$

$$NO + O_3 \overset{k_3}{\rightarrow} NO_2 + O_2 \qquad (R3)$$

235   The actinometric experiments were carried out at eight different temperatures (213, 243, 263, 268, 273, 283, 295 and 296 K) in dry synthetic air, each with the highest light intensity setting possible, for long term use. Figure 4a shows pressure, temperature and the concentrations of the trace gases of one of these experiments. Please note that the instantaneous steps of 0.1 K in temperature when switching on and off the light is due to radiative heating of the sensors inside the chamber but not reflecting a sudden change in gas temperature. After turning on the light the NO_2-concentration decreases and the NO- and
240   O_3-concentration rise, the system reaches a dynamic equilibrium after 10-12 min. Using the equilibrium concentrations and assuming a quasi-stationary state for ozone, the photolysis frequency is calculated by using the following equation and the reaction rate constant $k_3 = 2.07 \times 10^{-12} \exp(-1400K/T)$ [$cm^3 molecule^{-1}s^{-1}$] as recommended by IUPAC (Atkinson et al., 2004).

$$j(NO_2) = k_3 \frac{[O_3][NO]}{[NO_2]} \tag{1}$$

The resulting photolysis frequencies for the different temperatures are shown in Fig. 4b. They vary slightly, resulting in a mean

245   value of $(1.58 \pm 0.21 \, (1\sigma)) \times 10^{-3} \, s^{-1}$. Additionally, one experiment was done in pure nitrogen but leading to very similar results. In comparison, the maximum values for a clear winter and a summer day in Karlsruhe are $3.4 \times 10^{-3} \, s^{-1}$ and $6.0 \times 10^{-3} \, s^{-1}$ (calculated with the Quick TUV Calculator of NCAR UCAR). Thus, one hour of illumination in the AIDA chamber corresponds to half an hour solar illumination on a clear winter day at ground level. Regarding the size of the chamber, this is a significant value. The biggest chamber of PACS-C3 (27 m³) at Paul Scherrer Institute in Switzerland achieves a NO_2

250   photolysis frequency of $2.0 \times 10^{-3} \, s^{-1}$ by combining arc xenon lamps and black-light lamps (Paulsen et al., 2005). By using three 4 kW high-pressure arc xenon lamps for the CESAM-chamber (4.2 m³) at the Interuniversiary Laboratory of Atmospheric Systems in Paris a photolysis frequency of $4.2 \times 10^{-3} \, s^{-1}$ is achieved (Wang et al., 2011). Since the chamber is higher than other chambers compared to the base area and the LED emissions are conical, uniform and intense illumination is particularly difficult. Being at the lower end of the illumination intensities still significant improvements based on the fast

255   development of LEDs in the near future seems possible.
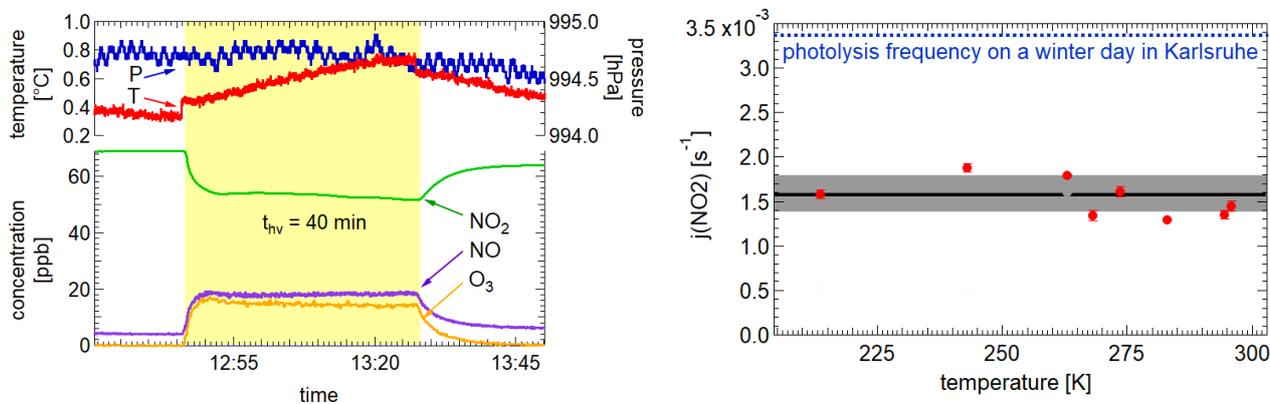
Figure 4: Pressure, temperatures and concentrations during an actinometric experiment with NO₂. The resulting photolysis frequencies at the different temperatures.

260   By constructing the light source as a combination of LEDs we achieved an illumination with a similar spectral distribution as the solar light at ground level as well as intensities which allow to simulate realistic conditions of the atmospheric illumination. Furthermore the light source has only a small impact on the temperature stability of the chamber. The average gas temperature increases by 0.7 K per hour for the first 2 hours of illumination with maximum power. This ensures stable simulation conditions and allows the illumination of clouds at relative humidities close to and above water or ice saturation. An example for this is

265   shown in Fig. S9. The light source itself can be operated safely between 183 K and 303 K and the irradiation spectrum can be changed at any point also during the experiments without technical difficulties. This is especially advantageous in comparison to xenon arc lamps which get very hot and are difficult to handle, for example if one would like to adjust the spectrum by

adding or removing a filter. Especially important for future uses is the light sources adaptability. LEDs can be replaced or added whenever there is a new technological development or scientific needs e.g. by adding UV-C LEDs.

5 Photolysis of 2,3-pentanedione

Studying the photolysis of 2,3-pentanedione in the gas phase demonstrates also the possibilities the new AIDA light source offers. 2,3-Pentanedione itself is a yellowish liquid which is used in the food industry for fragrance and flavouring (Burdock, 2002). But it is also emitted into the atmosphere through biological processes in vine and pine trees or formed by ozonolysis of alkenes (Burdock, 2002; Campo et al., 2006; Grossjean et al.;1998). Furthermore as an alpha carbonyl component, it can be used as a proxy for similar molecules. Carbonyl components can decompose in the atmosphere through photochemical pathways, forming radicals (Tadić et al., 2006). The primary photolysis step of 2,3-pentanedione can lead to different radicals with thresholds at around 340, 350, and 400 nm (Bouzidi et al. 2015; Szabo et al., 2011; Kercher et al., 2005). An overview of different reaction pathways for the photolysis of 2,3-pentanedione is given in Bouzidi et al. (2014 and 2015). Besides CO_2 and CO, the main products of these reaction pathways are acetaldehyde and formaldehyde (Szabo et al., 2011).

$$H_3C-\overset{\overset{O}{\|}}{C}-\overset{\overset{O}{\|}}{C}-CH_2-CH_3 \quad \xrightarrow{h\nu} \quad \cdots \quad \longrightarrow \quad H-\overset{\overset{O}{\|}}{C}-H \quad + \quad H_3C-\overset{\overset{O}{\|}}{C}-H$$

$C_5H_8O_2$
2,3-pentanedione

CH_2O
formaldehyde

C_2H_4O
acetaldehyde
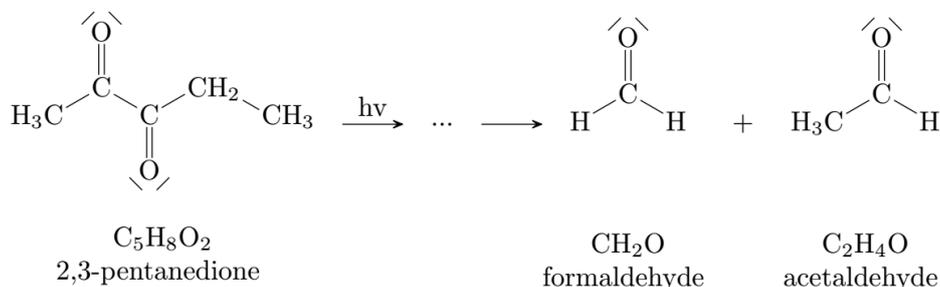
The aim is to improve the current knowledge about the decomposition behaviour of α–carbonyls and especially 2,3-pentanedione in the atmosphere. For this purpose photolysis frequencies and product distributions were determined as a function of temperature and wavelength of the irradiation.

5.1 Variation of temperature

The photolysis frequency j of a molecule is not only dependent on the incoming radiation I but also on the quantum yield φ, which for photolysis is defined by the actual number of bond cleavages divided by the number of absorbed photons, and the absorption cross section σ of the respective substance. The latter two as well as the product yields can be temperature dependent (Seinfeld and Pandis, 2006).

$$j = \int_{\lambda_1}^{\lambda_2} \sigma(\lambda,T)\Phi(\lambda,T)I(\lambda)\,d\lambda \tag{2}$$

As temperature dependencies of the photolysis of other components like NO_2 (Shetter et al., 1988), ozone (Smith et al., 2000) or o-methylacetophenon (Scaiano, 1980) are minor it is to be expected that this is also the case for 2,3-pentanedione. But as

acetylaldehyde and formaldehyde are not the direct photolysis products, a temperature dependence of their formation cannot

be ruled out. Thus the photolysis frequencies, quantum yields, and the product yields were determined in a series of

295   experiments at five different temperatures (213, 243, 273, 283, 298 K). Employing the PTR-MS the mass concentrations of

acetaldehyde and formaldehyde in the gas phase were measured (see Fig. S4 in supplement). The photolysis frequencies are

calculated by regarding the photolysis as a first-order reaction. This is justified as the data show a linear behaviour on a

logarithmic scale. The slope of the line allows to calculate the photolysis frequency for the respective experiment (see Fig. 5).

The concentration of 2,3-pentanedione decays due to photolysis but especially for the lower temperatures also due to the

300   adsorption of molecules from the gas phase at the chamber walls. To calculate the photolysis frequency (j_{PTD}) of 2,3-

pentanedione (PTD) the mean value of the decay before and after illumination (k_W) is subtracted from the decay during

illumination. As the slope is typically steeper before than after illumination, subtraction of the corresponding values instead of

the mean value give the maximum uncertainty for the resulting photolysis frequency.

$$\frac{d[PTD]}{dt} = -k\,[PTD] \Rightarrow \ln\frac{[PTD]_t}{[PTD]_0} = tk \tag{3}$$

305   $$k_W = \frac{k_{W\,before} + k_{W\,after}}{2} \rightarrow j_{PTD} = k - k_W \tag{4}$$
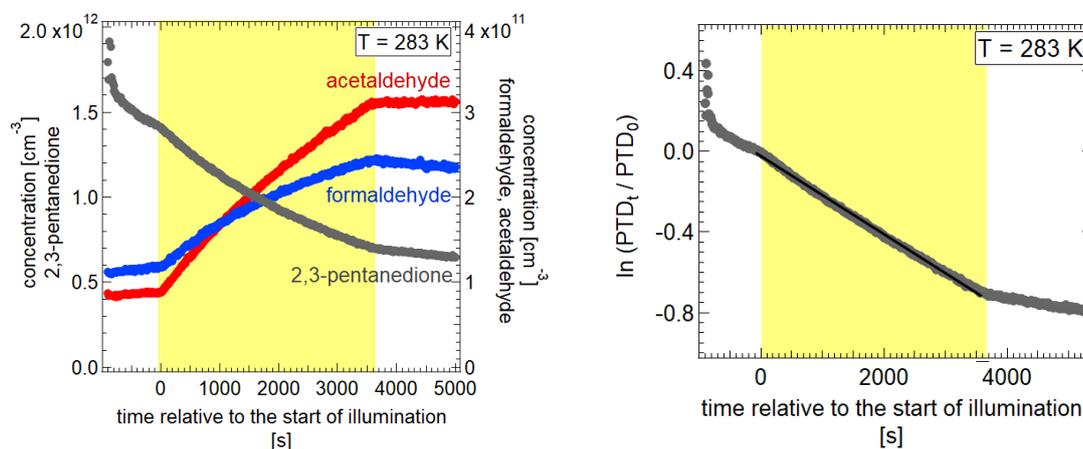
Figure 5: Concentrations of 2,3-pentanedione, acetaldehyde and formaldehyde during the experiment. Logarithmic depiction of the 2,3-pentandione (PTD) concentration to calculate the photolysis frequency.

310

The resulting photolysis frequencies and product yields are shown in Fig. 6 as a function of temperature. The photolysis

frequencies vary only slightly and there is no significant temperature dependence. The wall loss for the experiment at 213 K

before illumination resulted in a stronger concentration decrease compared to during the illumination. As a result only an upper

limit of photolysis frequency, calculated with the wall loss rate after the illumination is given in Fig. 6. It is safe to assume that

315   photolysis was taking place, even though it is difficult to define a frequency, because the formation of products could be

observed. The mean value for the four photolysis frequencies from 243 to 298 K is $(1.03 \pm 0.15\ (1\sigma) \times 10^{-4})$ s^{-1}. Regarding

photolysis of 2,3-pentanedione alone, this corresponds to an atmospheric lifetime of about 40 minutes on a summer day. The value for 298 K is not significantly different from the mean with $(1.24 \pm 0.12 \text{ x } 10^{-4})$ s^{-1}. Szabo et al. (2011) observed a photolysis frequency of 2,3-pentanedione of (1.40 ± 0.06) x 10^{-5} s^{-1} at 300 K. This is only 11 % of our measured value. There

320   are two distinct differences in the experimental setup which could explain the discrepancy. First is the fact that Szabo et al. (2011) were adding 1-pentene to trap OH radicals, which may be formed through photolysis of 2,3-pentanedione directly or by the photolysis of one of the reaction products. They account for a 30% higher photolysis frequency without 1-pentene. Second is the spectral difference of the light sources used. For the experiments of Szabo et al., a combination of two fluorescent tubes with emission maxima at 312 and 365 nm were used as light source. This results in a narrower spectrum overall.

325   Additionally the absorption spectrum of 2,3-pentanedion shows a minimum at 325 nm, thus the main photolysis was probably only driven by the emission of the fluorescent tube with a peak wavelength at 365 nm. Bouzidi et al. (2014) measured at 298 K a photolysis frequency of (3.6 ± 0.03) x 10^{-5} s^{-1} and (4.3 ± 0.03) x 10^{-5} s^{-1} with and without an OH radical scavenger. These are already higher values than the results of Szabo et al. But the value in absence of an OH radical scavenger is only 35% and hence significantly lower than the value we have observed. A major difference is that Bouzidi et al. (2014) uses 2,3-

330   pentanedione at concentrations of 12-48 ppm, while we use concentrations of 20 – 71 ppb. Thus it is possible that recombination process play a larger role than in our experiments. As for the experiments reported by Szabo et al., (2011) one major difference is the light source used (broadband UV lamps: 330-480 nm with a maximum near 370 nm).

The yields of the products of acetaldehyde and formaldehyde were determined, using a simple kinetic model applying the software KinSim (Peng and Jimenez, 2019) in Igor Pro. The model accounted for the wall loss of 2,3-pentanedione as well as

335   the photolysis and consecutive formation of formaldehyde and acetaldehyde with the yields x and y. The rate for the wall loss was set as the mean value k_W. The yields and the photolysis rates were fitted to the measured concentration profiles. The resulting product yields are shown in Fig. 6b, ignoring the experiment at 213 K due to the strong wall losses. The error bars reflect mainly the uncertainties implied by the wall losses, and to a smaller extent those of the quantification by the PTR-MS measurement. The yields for acetaldehyde are always higher than for formaldehyde and a strong positive temperature

340   dependence can be observed. As a temperature dependence of the photolysis itself can be ruled out the different yields have to be accounted for a change in the reaction mechanism. As there are a lot of possible pathways after the primary photolysis, either the reaction pathways to the formation of acetaldehyde and formaldehyde are thermodynamically controlled and decrease with temperature or other pathways are gaining in significance with lower temperatures. One of the formation reactions of formaldehyde in the reaction mechanism given by Bouzidi et al. (2014 and 2015) is the reaction of CH_3O with O_2.

345   Its reaction rate has been studied by several groups. These findings are summarised in Wantuck et al. (1987). According to their results the reaction rate at 293 K is 1.8 times the reaction rate at 243 K, which may explain our observed temperature dependence partially. For the formation of acetaldehyde the reaction of C_2H_5O with O_2 is an important pathway and its reaction rate has been studied by Hartmann et al. (1990) for temperatures between 295 and 411 K. Their expression for the reaction rate implies a 1.5 higher reaction rate for 293 K than for 243 K. Even though the expression might not be perfect for lower

350   temperatures, it shows that the temperature dependence for this reaction pathway may also be considered as explanation for

our observations. For a temperature of 298 K and without OH radical scavenger Bouzidi et al. (2014) reports yields 0.41 ± 0.7, 0.39 ± 0.6 and 7.6 ± 0.005 for formaldehyde, acetaldehyde, and CO, respectively. The yield for formaldehyde agrees with our observation but the yield for acetaldehyde is significantly lower than the value observed in the AIDA experiments. This may be due to the different analytical techniques used (PTR-MS vs. derivatization followed by HPLC-UV analysis), the different

355   light sources or different wall loss rates in the different simulation chambers.
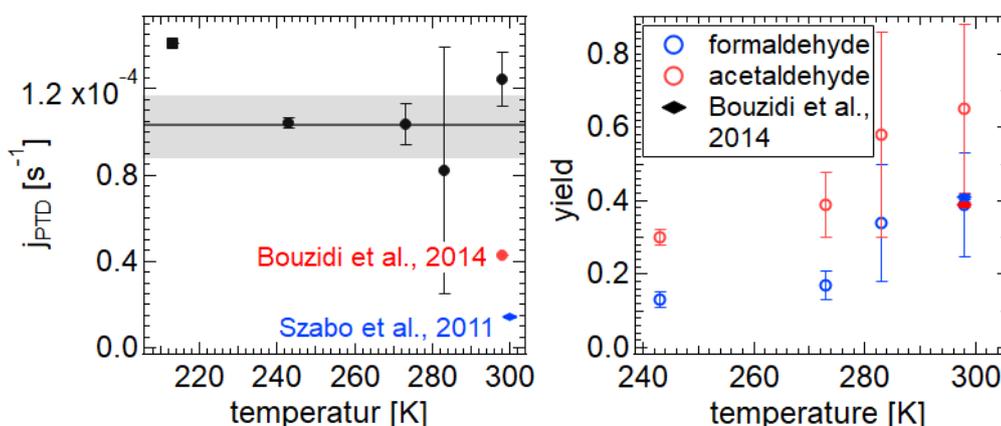
Figure 6: Left: Photolysis frequencies of the photolysis of 2,3-pentanedione for the experiments at different temperatures and the photolysis frequencies measured by Szabo et al. (2011) and Bouzidi et al. (2014). Right: The product yields for the corresponding experiments. The wall loss at 213 K was too high to perform a model run for the product yield. The photolysis frequency for this
360   **temperature shown in the figure is the upper limit with the assumption of a minimal wall loss, equivalent to the value after illumination.**

5.2 Variation of the irradiation spectrum

In addition to the temperature dependent experiments 2,3-pentanedione was illuminated in intervals of 15 min at 298 K by changing the spectrum of the emitted light. The different spectra are given in Fig. S4. This was achieved by using only a part
365   of the LEDs. The aim was to evaluate the wavelength dependence of the photolysis. Furthermore, the results were used to determine a quantum yield of the photolysis. Figure 7 shows the evolution of the 2,3-pentanedione concentration during this experiment. The yellow parts represent the illumination periods with the corresponding peak wavelengths of the LEDs used for each illumination. It should be noted that the resulting spectrum is always broader than the specified peak wavelength (see Fig. S4). For a spectrum which is comprised of the LEDs with the peak wavelengths from 365 nm to 528 nm the resulting
370   spectrum has an intensity of about 50% from 360 nm to 533 nm as the FWHM for most LEDs is between 10 and 15 nm. The concentration profile shows that there is no significant photolysis detectable with solely the UV-LEDs in use. This is to be expected regarding the minimum of the absorption spectrum of 2,3-pentanedione between 300 and 350 nm. On the other hand the largest impact has the addition of the LEDs with peak wavelengths of 455, 415 and 405 nm. This is also the region were the absorption spectrum shows a maximum (see Fig. 8). The values for the photolysis frequencies are summarized in Table 1.
375   It is noteworthy that we can still measure a significant photolysis of 2,3-pentanedione even with an illumination produced of

LEDs with peak wavelengths well beyond the photolysis threshold of 400 nm. In particular, this applies to the illumination periods marked as 455 - 528 nm and 475 – 528 nm.
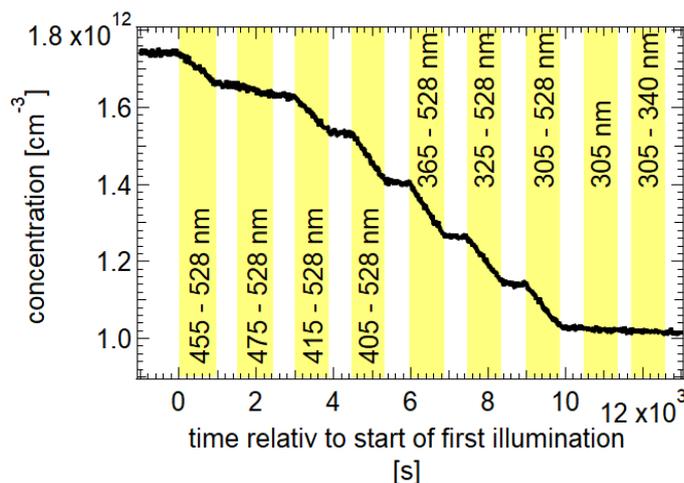
Figure 7: Concentration of 2,3-pentanedione over the course of several illumination periods with different wavelength
380 **ranges of light spectra irradiated at 298 K.**

The determination of the quantum yield requires a comparison of the calculated photolysis frequency with the quantum yield equal to one with the observed values (see Table 1). As the photolysis frequency can be calculated as the sum over the discrete values of the radiant flux $J(\lambda)$, the absorption cross section $\sigma(\lambda)$ and the quantum yield $\phi(\lambda)$ the actual quantum yield can be
385 calculated.

$$j_{PTD} = \sum_{\lambda_{start}}^{\lambda_{end}} \sigma(\lambda) \, \varphi(\lambda) J(\lambda) \tag{5}$$

$$\Rightarrow \Phi = \frac{j_{PTD_{observed}}}{j_{PTD_{calculated}}} \tag{6}$$

It should be kept in mind that this value is only valid for our experimental conditions, this includes the illumination conditions
390 but also chamber specific influences like wall loss effects. One way of accounting for this is to normalise the value with $j_{NO2,calc.}/j_{NO2}$ as it was done by Bouzidi et al. (2014) which will be discussed in the following.

The quantum yield is not calculated if only the long wavelengths from 475 to 528 nm are used or if only the short wavelengths from 305 to 340 nm are used. This is firstly due to the absorption spectrum of 2,3-pentanedione being only available until 450 nm (Szabó et al., 2011). Even with a reasonable extrapolation up to 500 nm the comparison between the photolysis frequencies
395 for the spectral range of 450 to 500 nm is not valid as the LEDs with a peak wavelength of 528 nm are ignored. Secondly, due to the minimum in the absorption spectrum in the UV-region the simplification to use a spectrum from 300 to 345 nm when using LEDs with peak wavelengths from 305 to 340 nm is underestimating the actual available light. This is true for the complete spectral width but more drastic were the actual spectrum overlaps with the absorption maximum. Furthermore, the

given uncertainty for the absorption coefficient in the region of 330 nm is up to 40%, adding considerably to the uncertainty

400 at this wavelength range. Thus, only the values calculated for wavelengths between 300 and 500 nm were used for comparison, resulting in a mean quantum yield of 0.36 ± 0.04. There seems to be no obvious tendency of the quantum yield regarding the spectral characteristics in the respective wavelength range. Szabo et al., (2011) estimated a quantum yield of 0.41 ± 0.05 for the photolysis through solar irradiation and Bouzidi et al., (2014) a quantum yield of 0.20 ± 0.02 for illumination with fluorescent lamps. Considering the uncertainties there is a good agreement between the value determined by Szabo et al.,

405 (2011) and our experiments, while the value of Bouzidi et al. is about 56 % of our value. If we apply a correction according to the procedure used by Bouzidi et al. (2014) we result in a quantum yield of 0.45 ($j_{NO2,calc.}/j_{NO2} = 1.25$). Hence, the difference is then even larger.
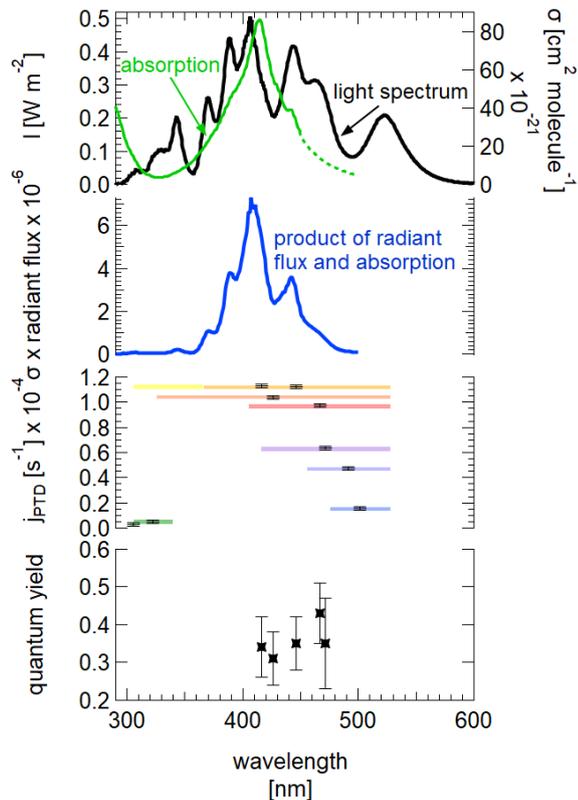
410 **Figure 8: Top: Measured spectrum of the light source at 3 m height inside the chamber. Absorption spectrum of 2,3-pentanedione, extrapolated for the part between 450 and 500 nm (Data: Szabó et al., 2011). Upper middle: Product of radiant flux and absorption spectrum. Bottom middle: Observed photolysis frequencies for the corresponding illumination at different wavelength ranges. Bottom: Calculated quantum yields for the corresponding wavelength ranges.**

415

calculated values		observed values		
λ [nm]	j_{PTD}	λ [nm]	j_{PTD}	φ
470-500	$(9.00\pm0.90)\times10^{-6}$	475-528	$(1.54\pm0.13)\times10^{-5}$	*
450-500	$(3.50\pm0.37)\times10^{-5}$	455-528	$(4.70\pm0.13)\times10^{-5}$	*
410-500	$(1.82\pm0.27)\times10^{-4}$	415-528	$(6.33\pm0.11)\times10^{-5}$	0.35 ± 0.12
400-500	$(2.24\pm0.35)\times10^{-4}$	405-528	$(9.71\pm0.13)\times10^{-5}$	0.43 ± 0.08
360-500	$(3.24\pm0.52)\times10^{-4}$	365-528	$(1.12\pm0.01)\times10^{-4}$	0.35 ± 0.07
320-500	$(3.32\pm0.54)\times10^{-4}$	325-528	$(1.04\pm0.01)\times10^{-4}$	0.31 ± 0.07
300-500	$(3.29\pm0.50)\times10^{-4}$	305-528	$(1.13\pm0.01)\times10^{-4}$	0.34 ± 0.08
300-310	$(7.84\pm1.64)\times10^{-7}$	305	$(2.61\pm1.36)\times10^{-6}$	*
300-345	$(3.85\pm1.36)\times10^{-6}$	305-340	$(5.04\pm1.41)\times10^{-6}$	*

Table 1: Measured and calculated photolysis frequencies of the photolysis of 2,3-pentanedione for different wavelength ranges as well as calculated quantum yields for a temperature of 298 K. The given wavelengths for the observed values refer to the peak wavelengths of the outmost activated LEDs. Values marked as * are not reliable because the difference between the estimated wavelength range and the actual spectral width is affecting the final results too strongly.

420

6 Photolysis of dissolved organic components

To explore the possibilities the light source at the AIDA chamber offers two further experimental series were conducted. One system studied is DTDP, a pyridine-derivative, as a proxy for atmospheric brown carbon components, diluted in aqueous

425 ammonium nitrate and ammonium sulphate solution droplets. A second system consists of ammonium nitrate solution particles, containing iron oxalate as a photosensitizer and pinonic and pinic acid as typical secondary organic components. For both systems only the main preliminary results are presented.

6.1 Photolysis of 3,5-diacetyl-2,4,6-trimethyl-1,4-dihydropyridine (DTDP)

DTDP, a pyridine-derivative, is known as an atmospheric brown carbon component (Kampf et al., 2016) which can be formed

430 e.g. by reaction of acetaldehyde and 2,4-pentanedione in the presence of ammonium sulphate. Its absorption spectrum shows a strong band around 380 nm (cf. Fig. S6). Therefore, we studied its photolysis in aqueous droplets containing ammonium nitrate and ammonium sulphate (weight ratios of DTDP:NH_4NO_3:$(NH_4)_2SO_4$ of 1:2:1) at the temperatures 264, 273, 283, and 293 K at relative humidities of 70-79 %. The dry diameter of the aerosol particles was 350 nm.

The illumination of these droplets leads to the depletion of DTDP in the particle phase corresponding to an average photolysis
435 frequency of $(6 \pm 6) \times 10^{-4}\,s^{-1}$ over all four temperatures (see Fig. S7). Even though the exact determination of the mass loadings
of DTDP in the particle phase turned out to be problematic, we can say that the estimated lifetime of DTDP regarding
photolysis in the atmosphere should be in the range of 7-15 minutes. During illumination the production of several components
in gas and particle phase could be observed. 16 of these components could be observed in the particle phase at all four
temperatures studied as well as in the gas phase for three of the experiments. The gas phase data for the fourth experiment is
440 not available due to technical problems. The mass increases for these 16 components at 293 K is given in the supplement. Two
of these could be identified as 3,5-diacetyl-2,4,6-trimethylpyridine (m/z 205.25) and 3,5-diacetyl-2,6-dimethyl-4-
hydropyridine (m/z 191.23) by comparison with results of Mitsunobu et al. (1971) and Memarian et al. (2004). Two stable
aromatic compounds formed through elimination of H_2, CH_3, respectively. The formation of these products is temperature
dependent as shown in Fig. 9 for the case of 3,5-diacetyl-2,4,6-trimethylpyridine. Further molecular structures e.g. by
445 elimination of CO are possible and a corresponding mass to charge ratio can be found, but a more detailed characterization
still needs to be done.
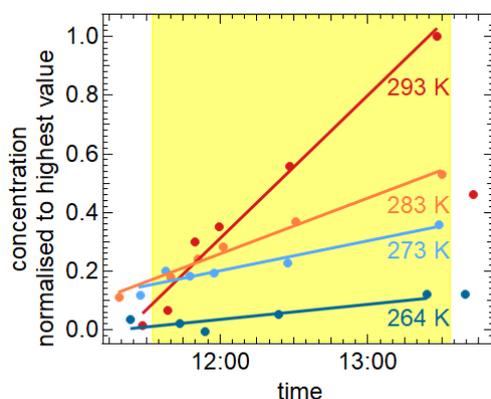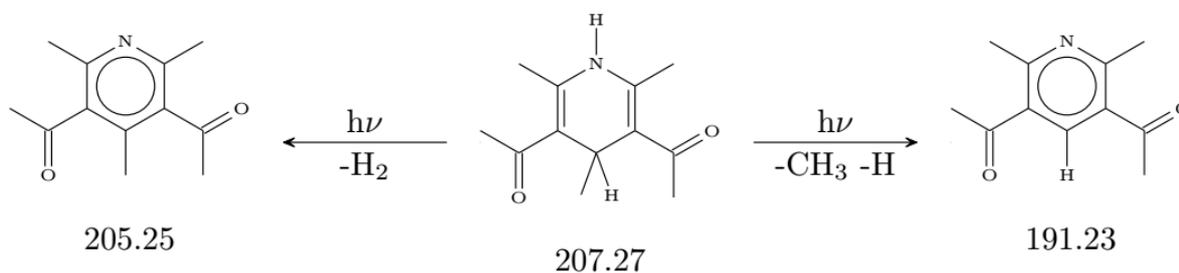
Figure 9: Mass increase over the illumination period of the mass peak at m/z = 205 in the particle phase, identified as 3,5-diacetyl-
450 **2,4,6-trimethylpyridine. Dots represent the measurement values. The formation is slower at lower temperatures.**

6.2 Depletion of pinic and pinonic acid by iron oxalate as photosensitizer

The illumination of iron oxalate charge-transfer-complexes leads to the production of radicals particularly OH radicals. Oxalic acid itself does not decompose through solar illumination. But through the complexation with Fe^{3+}-ions, absorption in

455 the UV and visible region is possible (Zuo and Hoigné, 1994; Cooper and DeGraff, 1971, Pozdnyakov et al., 2008). Detailed descriptions of the photolytic decomposition of the oxalic acid and the formation of radicals can be found in Chen et al. (2007 and 2008) and Pozdnyakov et al. (2008). The radicals can consequently react with water and the organic compounds in the aerosol particles. We studied the depletion of two organic acids in aqueous droplets containing also ammonium nitrate and iron oxalate at temperatures of 283, 243, and 213 K at relative humidities of 88, 72, and 55%, respectively. Pinonic and

460 pinic acids are well known oxidation products of α-pinen (Christoffersen et al., 1998; Yu et al. 1998) which is, alongside other terpenes, emitted into the atmosphere in large quantities (Guenther et al., 2012). The aerosol particles were generated by dispersing an aqueous solution of 0.0065 mol l^{-1} pinonic acid, 0.0073 mol l^{-1} pinic acid, 0.013 mol l^{-1} NH4NO3, and 0.0021 mol l^{-1} iron oxalate or 0,0081 mol l^{-1} oxalate in the reference experiment. The resulting dry particle diameters were 350 nm. Mass spectrometric data show a decrease in the concentrations of the two acids in the particle phase during

465 illumination, with the strongest decrease at the warmest temperature (283 K) (see Fig. 10) and a negligible concentration change for pinic acid at 213 K. Several masses increase during illuminations, of which three could be identified as $C_8H_{12}O_5$, $C_{10}H_{15}NO_6$ and $C_{10}H_{15}NO_7$ (see Fig. 10, last panel). Decomposition of pinic and pinonic acid as well as the formation of products reduce significantly with temperature, which might be partially due to the increased viscosity of the aerosol particles. The evolution of particle diameter, relative humidity and temperature for the experiment at 283 K can be found in

470 Fig. S8. A reference experiment at 283 K with oxalic acid, pinonic acid, and NH_4NO_3 shows no distinct reduction in the pinonic acid concentration during illumination. Our analysis results first order rate coefficients of 2-5 x 10^{-4} s^{-1} for the decay of pinonic acid at 283, 243 and 213 K as well as 3-5 x 10^{-4} s^{-1} for pinic acid at 283 and 243 K.
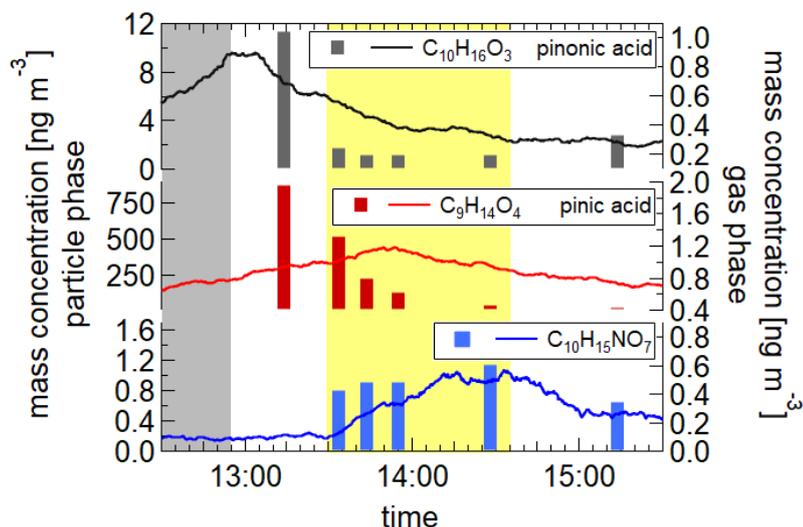
Figure 10: Mass concentration of pinic and pinonic acid, as well as one of the identified products. Bars: Particle phase; line: Gas
475 **phase; grey shading: Introduction of aerosol into the AIDA chamber; yellow: Illumination period. Pinic and pinonic acid reduce**
during illumination while the product $C_{10}H_{15}NO_7$ increases. Due to its instable peroxy structure the product concentration declines
after the end of the illumination.

These results demonstrate that iron oxalate acts as photosensitizer, which can potentially contribute to degradation of organic
480 compounds in aqueous aerosol particles.

7 Conclusions

With the construction of a light source for the AIDA chamber, aerosol formation and ageing studies as well as cloud processes
can now be extended including illumination with light of atmospherically relevant intensities and spectral characteristics. Light
intensities comparable to 25 % of a clear summer day or 44 % of a clear winter day in Karlsruhe are possible. This was achieved
485 by using a combination of LEDs with 11 different peak wavelengths from 305 nm to 528 nm, with the additional possibility
to change the irradiation spectrum and photon flux at any point during the experiments. Since the LEDs emit only very little
IR radiation the deterioration of the excellent temperature homogeneity of the simulation chamber is relatively small with 0.7
K/h. Therefore, the investigation of the interaction of light with gas phase components, aerosols as well as water and ice clouds
is now possible for simulated tropic to stratospheric conditions.
490 Characterization experiments show a photolysis frequency for NO_2 of $(1.59 \pm 0.20 \, (1\sigma)) \times 10^{-3} \, s^{-1}$ in the temperature range
between 213-295 K and a spectral shape similar to the solar spectrum in the UV-VIS range.
First experiments with 2,3-pentanedione prove the applicability of the light source at different temperatures and with different
irradiation spectra. The formation of the photolysis products acetaldehyde and formaldehyde show a distinct temperature
dependence with yields decreasing with decreasing temperature. The photolysis itself is independent of the temperature.
495 From the variation of the irradiation spectrum we conclude that the photolysis of 2,3-pentanedione is possible for wavelengths
below 460 nm with a mean photolysis frequency of $(1.03 \pm 0.15) \times 10^{-4} \, s^{-1}$. The quantum yield for the photolysis was
determined as 0.36 ± 0.04.
Further experiments with a photosensitizer and brown carbon components show the variability in photo-aging experiments
now possible in the AIDA chamber as well as first results. This includes an estimate for the atmospheric lifetime of 3,5-
500 diacetyl-2,4,6-trimethyl-1,4-dihydropyridine of 11±4 min and the identification of the photolysis products 3,5-diacetyl-2,4,6-
trimethylpyridine an 3,5-diacetyl-2 ,6-dimethylpyridine. Additionally a temperature dependent degradation of organic acids in
aqueous droplets through the photosensitizer iron-oxalate could be observed.
Although, the light source so far only generates about 1/3 of the maximum solar irradiation at ground level with a substantial
intensity gradient throughout the simulation chamber it could be shown that this type of light source allows reproducible

505 experiments over a wide range of simulated atmospheric conditions and with a large flexibility and control of the irradiation spectrum. A specific asset of the setup is the large temperature range, over which the studies can be conducted.

Supplement

The supplement related to this article is available online at:…

510

Author contributions

M.V. and J.N. build the light source based on ideas by H.S. and T.L. M.V. and H.S. conducted the experiments with substantial contributions by L.G. (AMS & CIMS), F.J. (filter samples, absorption measurements), and J.S. (AMS & PTR-MS). The data were analysed by H.S. and M.V. (light spectra, CIMS, aerosol data), J.S. (AMS & PTR-MS), B.K. (kinetics). M.V. wrote the

515 manuscript with contributions from all co-authors.

Competing interests

The authors declare that they have no conflict of interest.

520 **Acknowledgements**

The authors also want to thank the staff of the KIT-IMK-AAF especially Georg Scheurig, Tomasz Chudy, and Steffen Vogt for their technical support. A special thanks is going to GRACE, the graduate school of KIT for financing conferences and the aerosol summer school.

525 **Financial support**

This project/work has received funding from the European Union's Horizon 2020 research and innovation programme through the EUROCHAMP-2020 Infrastructure Activity under grant agreement No 730997.

Data availability

530 The AIDA light spectrum is available via the KITopen data repository (link/doi).

References

Aregahegn, K. Z., Nozière, B., George, C.; Organic aerosol formation photo-enhanced by the formation of secondary photosensitizers in aerosols, Faraday Discuss., 165, 123-134, doi: 10.1039/c3fd00044c, 2013.

Atkinson, R., Baulch, D. L., Cox, R. A., Crowley, J. N., Hampson, R. F., Hynes, R. G., Jenkin, M. E., Rossi, M. J., Troe, J.;

535 IUPAC Task Group on Atmospheric Chemical Kinetic Data Evaluation, Atmos. Chem. Phys., 4, 1461, 2004.

Atkinson, R., Baulch, D. L., Cox, R. A., Crowley, J. N., Hampson, R. F., Hynes, R. G., Jenkin, M. E., Rossi, M. J., Troe, J.; Evaluated kinetic and photochemical data for atmospheric chemistry: Volume II - Gas phase reactions of organic species, Atmos. Chem. Phys., 6, 3625-4055, doi: 10.5194/acp-6-3625-2006, 2006.

Bartl, J., Baranek, M.; Emissivity of aluminium and its importance for radiometric measurement, Meas. Sci. Rev., 4, 31-36,
540   2004.

Baltrusaitis, J., Schuttlefield, J., Jensen, J. H., Grassian, V. H.; FTIR spectroscopy combined with quantum chemical calculations to investigate adsorbed nitrate on aluminium oxide surfaces in the presence and absence of co-adsorbed water, Phys. Chem. Chem. Phys., 9, 4970-4980, doi: 10.1039/b705189a, 2007.

Bohn, B., Zilken, H.; Model-aided radiometric determination of photolysis frequencies in a sunlit atmosphere simulation
545   chamber, Atmos. Chem. Phys., 5, 191-206, doi: 10.5194/acp-5-191-2005, 2005.

Bouzidi, H., Fittschen, C., Coddeville, P., Tomas, A.; Photolysis of 2,3-pentanedione and 2,3-hexanedione: Kinetics, quantum yields, and product study in a simulation chamber, Atmos. Environ., 82, 250-257, doi: 10.1016/j.atmosenv.2013.10.039, 2014.

Bouzidi, H., Djehiche, M., Gierczak, T., Morajkar, P., Fittschen, C., Coddeville, P., Tomas, A., Low-Pressure Photolysis of 2,3-Pentanedione in Air: Quantum Yields and Reaction Mechanism, 119, 12781-12789, doi: 10.1021/acs.jpca.5b09448, 2015.

550   Burdock G. A.; Fenaroli's handbook of flavor ingredients, CRC press, 4th edition, S.1411-1412, 2002.

Campo, E., Ferreira, V., Escudero, A., Marqués, J. C., Cacho, J.; Quantitative gas chromatography-olfactometry and chemical quantitative study of the aroma of four Madeira wines, Analytica Chimica Acta, 563, 180-187, doi: 10.1016/j.aca.2005.10.035, 2006.

Chen, J., Zhang, H., Tomov, I. V., Wolfsberg, M., Ding, X., Rentzepis, P. M.; Transient structures and kinetics of the
555   ferrioxalate redox reaction studied by time-resolved EXAFS, optical spectroscopy, and DFT, J. Phys. Chem. A, 111, 9326-9335, doi: 10.1021/jp0733466, 2007.

Chen, J., Zhang, H., Tomov, I. V., Rentzepis, P. M., Electron transfer mechanism and photochemistry of ferrioxalate induced by excitation in the charge transfer band, Inorg. Chem., 47, 2024-2032, doi: 10.1021/ic7016566, 2008.

Christoffersen, T. S., Hjorth, J., Horie, O., Jensen, N. R., Kotzias, D., Molander, L. L., Neeb, P., Ruppert, L., Winterhalter, R.,
560   Virkkula, A., Wirtz, K., Larsen, B. R.; Cis-pinic acid, a possible precursor for organic aerosol formation from ozonolysis of α-pinene, Atmos. Environ., 32, 1657-1661, doi: 10.1016/S1352-2310(97)00448-2, 1998.

Ciuraru, R., Fine, L., Pinxteren, M. V., D'Anna, B, Herrmann, H, George, C.; Unravelling New Processes at Interfaces: Photochemical Isoprene Production at the Sea Surface, Environ. Sci. Technol, 49, 13199-13205, doi: 10.1021/acs.est.5b02388, 2015.

565   Cooper, G. D., DeGraff, B. A.; Photochemistry of the ferrioxalate system, J. Phys. Chem., 75, 2897-2902, 1971.

Fu, H., Ciuraru, R., Dupart, Y., Passananti, M., Tinel, L., Rossignol, S., Perrier, S., Donaldson, J. D., Chen, J., George, C.; Photosensitized Production of Atmospherically Reactive Organic Compounds at the Air/Aqueous Interface, JACS, 137, 8348-8351, doi: 10.1021/jacs.5b04051, 2015.

George, C., Ammann, M., D'Anna, B., Donaldson, D. J., Nizkorodov, S. A.; Heterogeneous Photochemistry in the Atmosphere,
570   Chem. Rev., 115, 4218-4258, doi: 10.1021/cr500648z, 2015.

Goldstein, A. H., Galbally, I. E.; Known and unexplored organic constituents in the earth's atmosphere, Eviron. Sci. Techn.,
41, 1514-1421, doi: 10.1021/es072476p, 2007.

Grosjean, E., Grosjean, D.; The gas-phase reaction of alkenes with ozone: Formation yields of carbonyls from biradicals in
ozone-alkene-cyclohexane experiments, Atmos. Environ., 32, doi: 10.1016/S1352-2310(98)80005-8, 1998.

575   Guenther, A. B., Jiang, X., Heald, C. L., Sakulyanontvittaya, T., Duhl, T., Emmons, L. K., Wang, X.; The model of emissions
of gases and aerosols from nature version 2.1 (MEGAN2.1): An extended and updated framework for modeling biogenic
emissions, Geosci. Model Dev., 5, 1471-1492, doi: 10.5194/gmd-5-1471-2012, 2012.

Hartmann, D., Karthäuser, J., Sawerysyn, J. P., Zellner, R.; Kinetics and HO2 Product Yield of the Reaction C2H5O + O2
between 295 and 411 K, Ber. Bunsenges. Phys. Chem., 94, 639-645, doi: 10.1002/bbpc.19900940604, 1990.

580   Harvey, R. B., Stedmann, D. H., Chameides, W.; Determination of the Absolute Rate of Solar Photolysis of NO$_2$, J. Air. Pollut.
Acontrol Assoc., 27, 663-666, doi:10.1080/00022470.1977.10470469, 1977.

Herrmann, H., Schaefer, T., Tilgner, A., Styler, S. A., Weller, C., Teich, M., Otto, T.; Tropospheric Aqueous-Phase Chemistry:
Kinetics, Mechanisms, and Its Coupling to a Changing Gas Phase, Chem. Rev., 115, 4259-4334, doi: 10.1021/cr500447k,
2015.

585   Holmes, J. R., O'Brien, R. J., Crabtree, J. H., Hecht, T. A., Seinfeld, J. H.; Measurement of Ultraviolet Radiation Intensity in
Photochemical Smog Studies, Environ. Sci. Technol., 7, 519-523, doi: 10.1021/es60078a002, 1973.

Fankhauser A. M., Bourque, M., Almazan, J., Marin, D., Fernandez, L., Hutheesing, R., Ferdousi, N., Tsui, W. G., McNeill,
V. F.; Impact of Environmental Conditions on Secondary Organic Aerosol Production from Photosensitized Humic Acid,
Environ. Sci. Technol., 54, 5385-5390, doi:10.1021/acs.est.9b07485, 2020.

590   Kampf, C. J., Filippi, A., Zuth, C., Hoffmann, T., Opatz, T.; Secondary brown carbon formation via the dicarbonyl imine
pathway : nitrogen heterocycle formation and synergistic effects, Phys. Chem. Chem. Phys., 18, 18353-18364, doi:
10.1039/C6CP03029G, 2016.

Kercher, J. P., Fogleman, E. A., Koizumi, H., Sztáray, B., Baer, T.; Heats of formation of the propionyl ion and radical and
2,3-pentanedione by threshold photoelectron photoion coincidence spectroscopy, J. Phys. Chem. A, 109, 939-946, doi:
595   10.1021/jp0458497, 2005.

Lehtipalo, K., Yan, C., Dada, L., Bianchi, F., Xiao, M., Wagner, R., Stolzenburg, D., Ahonen, L. R., Amorim, A., Baccarini,
A., Bauer P. S., Baumgartner, B., Bergen, A., Bernhammer, A.-K., Breitenlechner, M., Brilke, S., Buchholz, A., Stephany
Buenrostro Mazon, S., Chen, D., Chen, X., Dias, A., Dommen, J., Draper, D. C., Duplissy, J., Ehn, M., Finkenzeller, H.,
Fischer, L., Frege, C., Fuchs, C., Garmash, O., Gordon, H., Hakala, J., He, X., Heikkinen, L., Zeinritzi, M., Helm, J. C.,
600   Hofbauer, V., Hoyle, C. R., Jokinen, T., Kangasluoma, J., Kerminen, V.-M., Kim, C., Kirkby, J., Kontkanen, J., Kürten, A.,
Lawler, M. J., Mai, H., Mathot, S., Mauldin R. L., Molteni, U., Nichman, L., Nie, W., Nieminen, T., Ojdanic, A., Onnela, A.,
Passananti, M., Petäjä, T., Piel, F., Pospisilova, V., Quéléver, L. L. J., Rissanen, M P., Rose, C., Sarnela, N., Schallhart, S.,

Schuchmann, S., Sengupta, K., Simon, M., Sipilä, M., Tauber, C., Tomé, A., Tröstl, J., Väisänen, O., Vogel, A. L., Volkamer, R., Wagner, A. C., Wang, M., Weitz, L., Wimmer, D., Ye, P., Ylisirniö, A., Zha, Q., Carslaw, K. S., Curtius, J., Donahue, N. M., Flagan, R. C., Hansel, A., Riipinen, I., Virtanen, A., Winkler, P. M., Baltensperger, U., Kulmala, M., Worsnop, D. R.; Multicomponent new particle formation from sulfuric acid, ammonia, and biogenic vapors, Sci. Adv., 4, doi: 10.1126/sciadv.aau5363, 2018.

Memarian, H. R., Bagheri, M., Döpp, D.; Synthesis and photochemistry of novel 3,5-diacetyl-1,4-dihydropyridines. II [1], Monatshefte für Chemie, 135, 833-838, doi: 10.1007/s00706-003-0139-5, 2004.

Mitsunobu, O., Matsumoto, S., Wada, M., Masuda, H.; Photooxidation of 1,4-Dihydropyridines, Bulletin of the Chemical Society of Japan, 45, 1453-1457, 1972.

Möhler, O., Stetzer, O., Schäfers, S., Linke, C., Schnaiter, M., Tiede, R., Saathoff, H., Krämer, M., Mangold, A., Budz, P., Zink, P., Schreiner, J., Mauersberger, K., Haag, W., Kärcher, B., Schurath, U.; Experimental investigation of homogeneous freezing of sulphuric acid particles in the aerosol chamber AIDA, Atmos. Chem. Phys., 2, 211-223, doi: 10.5194/acp-3-211-2003, 2003.

Monge, M. E., Rosenørn, T., Favez, O., Müller, M., Adler, G., Riziq, A. A., Rudich, Y., Herrmann, H., George, C., D'Anna, B.; Alternative pathway for atmospheric particles growth, PNAS, 109, 6840-6844, doi: 10.1073/pnas.1120593109, 2012.

Müller, L., Reinnig, M.-C., Naumann, K. H., Saathoff, H., Mentel, T.F., Donahue, N. M. and Hoffmann, T.: Formation of 3-methyl-1,2,3-butanetricarboxylic acid via gas phase oxidation of pinonic acid – a mass spectrometric study of SOA aging, Atmos. Chem. Phys., 12, 1483-1496, doi:10.5194/acp-12-1483-2012, 2012.

Navea, J.G., Grassian, V.H.; Photochemistry of Atmospheric Particles, Encyclopedia of Interfacial Chemistry: Surface Science and Electrochemistry, 1-10, doi: 10.1016/B978-0-12-409547-2.13210-X, 2017.

Paulsen, D., Dommen, J., Kalberer, M., Prévôt, A.S.H., Richter, R., Sax, M., Steinbacher, M., Weingartner, E., Baltensperger, U., Secondary organic aerosol formation by irradiation of 1,3,5- trimethylbenzene-NO$_x$-H$_2$O in a new reaction chamber for atmospheric chemistry and physics, Environ. Sci. Technol., 39, 2668-2678, doi: 10.1021/es0489137, 2005.

Peng, Z., Jimenez, J. L.; KinSim: A Research-Grade, User-Friendly, Visual Kinetics Simulator for Chemical-Kinetics and Environmental-Chemistry Teaching, J. Chem. Educ., 96, 806-811, doi: 10.1021/acs.jchemed.9b00033, 2019.

Platt, S. M., El Haddad, I., Zardini, A. A., Clairotte, M., Astorga, C., Wolf, R., Slowik, J. G., Temime-Roussel, B., Marchand, N., Ježek, I., Drinovec, L., Močnik, G., Möhler, O., Richter, R., Barmet, P., Bianchi, F., Baltensperger, U., Prévôt, A. S. H.; Secondary organic aerosol formation from gasoline vehicle emissions in a new mobile environmental reaction chamber, Atmos. Chem. Phys., 13, 9141-9158, doi: 10.5194/acp-13-9141-2013, 2013.

Pozdnyakov, I. P., Kel, O. V., Plyusnin, V. F., Grivin, V. P., Bazhin, N. M.; New insight into photochemistry of ferrioxalate, J. Phys. Chem. A, 112, 8316-8322, doi: 10.1021/jp8040583, 2008.

Reeser, D. I., George, C, Donaldson, D. J.; Photooxidation of halides by chlorophyll at the air-salt water interface, J. Phys. Chem. A, 113, 8591-8595, doi: 10.1021/jp903657j, 2009.

Ren, Y., Grosselin, B., Daële, V., Mellouki, A., Investigation of the reaction of ozone with isoprene, methacrolein and methyl vinyl ketone using the HELIOS chamber, Faraday Discuss., 200, 289-311, doi: 10.1039/c7fd00014f, 2017.

Rohrer, F., Bohn, B., Brauers, T., Brüning, D., Johnen, F. J., Wahner, A., Kleffmann, J.; Characterisation of the photolytic HONO-source in the atmosphere simulation chamber SAPHIR, Atmos. Chem. Phys, 5, 2189-2201, doi: 10.5194/acp-5-2189-

640   2005, 2005.

Romano, A., Capozzi, V., Spano, G., Biasioli, F.; Proton transfer reaction–mass spectrometry: online and rapid determination of volatile organic compounds of microbial origin, Appl. Microbiol. Biotechnol., 99, 3787-3795, doi: 10.1007/s00253-015-6528-y, 2015.

Rossignol, S., Aregahegn, K. Z., Tinel, L., Fine, L., Nozière, B., George, C.; Glyoxal induced atmospheric photosensitized

645   chemistry leading to organic aerosol growth, Environ. Sci.Technol., 48, 3218-3227, doi: 10.1021/es405581g, 2014.

Rubasinghege, G., Grassian, V. H.; Photochemistry of adsorbed nitrate on aluminum oxide particle surfaces, J. Phys. Chem. A, 27,7818-7825, doi: 10.1021/jp902252s, 2009.

Saathoff, H., Möhler, O., Schurath, U., Kamm, S., Dippel, B. and Mihelcic, D.; The AIDA soot aerosol characterisation campaign 1999, Aerosol Science, 34, 1277 – 1296, doi:10.1016/S0021-8502(03)00363-X, 2003.

650   Saathoff, H. Naumann, K.-H., Möhler, O., Jonsson, Å. M., Hallquist, M., Kiendler-Scharr, A., Mentel, Th. F., Tillmann, R., Schurath, U.; Temperature dependence of yields of secondary organic aerosols from the ozonolysis of α-pinene and limonene, Atmos. Chem. Phys., 9, 1551-1577, doi: 10.5194/acp-9-1551-2009, 2009.

Scaiano, J C., Temperature dependence of the photochemistry of o-methylacetophenone. A laser flash photolysis study., Chem. Phys. Lett., 73, 319-322, doi: 10.1016/0009-2614(80)80381-2, 1980.

655   Seinfeld J. H., Pandis, S. P.; Atmospheric Chemistry and Physics From Air Pollution to Climate Change, John Wiley & Sons, Hoboken, New Jersey, 2nd edition, 116-117, 2006.

Sharpless, C. M., Blough, N. V.; The importance of charge-transfer interactions in determining chromophoric dissolved organic matter (CDOM) optical and photochemical properties, Environ. Sci.: Processes Impacts, 16, 654-671, doi: 10.1039/c3em00573a, 2014.

660   Shetter, R. E., Davidson, J. A., Cantrell, C. A., Burzynski Jr., N. J., Calvert, J. G.; Temperature dependence of the atmospheric photolysis rate coefficient for NO_2, JGR Atmospheres, 93, 7113-7118, doi: 10.1029/JD093iD06p07113, 1988.

Smith, G. D., Molina, L. T., Molina, M. J.; Temperature dependence of O(1D) quantum yields from the photolysis of ozone between 295 and 338 nm, J. Phys. Chem. A, 104, 8916-8921, doi: 10.1021/jp001006d, 2000.

Stocker T. F., Qin, D., Plattner, G.-K., Tignor, M., Allen, K. S., J.Boschung, Nauels, A., Xia, Y., Bex, V., Midgley, M. P.;

665   CLIMATE CHANGE 2013, The Physical Science Basis. Contribution of Working Group 1 to the Fifth Assessment Report of the Intergovernmental Panel on Climate Change, Cambridge University Press, Cambridge, 1-2228, 2013.

Szabó, E., Djehiche, M., Riva, M., Fittschen, C., Coddeville, P., Sarzyński, D., Tomas, A., Dóbé, S.; Atmospheric chemistry of 2,3-pentanedione: Photolysis and reaction with OH radicals, J. Phys. Chem. A, 115, 9160-9168, doi:10.1021/jp205595c, 2011.

670   Tadić, J., Moortgat, G. K., Wirtz, K.; Photolysis of glyoxal in air, Journal of Photochemistry and Photobiology A: Chemistry, 177, 116-124, doi: 10.1016/j.jphotochem.2005.10.010, 2006.

Wagner, R., Bunz, H., Linke. C., Möhler, O., Naumann, K.-H., Saathoff, H. Schnaiter, M., Schurath, U.; Chamber Simulations of Cloud Chemistry: The AIDA Chamber, In: Barnes, I., Rudzinky, K. J. (eds), Nato Science Series: IV: Earth an Environmental Science, Springer, Dordrecht, 62, doi: 10.1007/1-4020-4232-9_5, 2006.

675   Wang, J., Doussin, J. F., Perrier, S., Perraudin, E., Katrib, Y., Pangui, E., Picquet-Varrault, B.; Design of a new multi-phase experimental simulation chamber for atmospheric photosmog, aerosol and cloud chemistry research, Atmos. Meas. Tech., 4, 2465-2494, doi: 10.5194/amt-4-2465-2011, 2011.

Wantuck, P. J., Oldenburg, R. C., Baughcum, S. L., Winn, K. R.; Removal Rate Constant Measurements for CH3O by O2 over the 298-973 K Range, J. Phys. Chem., 91, 4653-4655, doi: 10.1021/j100302a004, 1987.

680   Wiesen, P.; Photooxidant Studies Using the European Photoreactor EUPHORE, Transp. Chem. Transform. Troposph., 2, 155-162, doi:10.1007/978-3-642-56722-3_25, 2001.

Yu, J., Flagan, R. C., Seinfeld, J. H.; Identification of products containing -COOH, -OH, and -C=O in atmospheric oxidation of hydrocarbons, Environ. Sci. Technol., 32, 2357-2370, doi: 10.1021/es980129x, 1998.

Yuan, B., Koss, A. R., Warneke, C., Coggon, M., Sekimoto, K., de Gouw, J. A.; Proton-Transfer-Reaction Mass Spectrometry:
685   Applications in Atmospheric Sciences, Chem. Rev., 117, 13187−13229, doi: 10.1021/acs.chemrev.7b00325, 2017.

Zádor, J., Turányi, T., Wirtz, K., Pilling, M. J.; Measurement and investigation of chamber radical sources in the European Photoreactor (EUPHORE), J. Atmos. Chem., 55, 147-166, doi: 10.1007/s10874-006-9033-y, 2006.

Zuo, Y., Hoigné, J.; Photochemical decomposition of oxalic, glyoxalic and pyruvic acid catalysed by iron in atmospheric waters, Atmos. Environ., 28, 1231-1239, doi: 10.1016/1352-2310(94)90270-4, 1994.

690

695

700